Bolgiano-Obukhov scaling in two-dimensional Rayleigh-Bénard convection at extreme Rayleigh numbers

Roshan Samuel [1,*] and Mahendra K. Verma [2,†]
[1] *Department of Mechanical Engineering, Indian Institute of Technology, Kanpur 208016, India*
[2] *Department of Physics, Indian Institute of Technology, Kanpur 208016, India*

(Received 1 March 2023; accepted 5 January 2024; published 16 February 2024)

Understanding the behavior of the kinetic energy spectrum and flux in two-dimensional (2D) turbulent thermal convection remains a challenge. In this paper, using high-resolution direct numerical simulation of Rayleigh-Bénard convection for Rayleigh numbers 10^{11}–10^{14} and unit Prandtl number, we show that 2D turbulent convection exhibits Bolgiano-Obukhov scaling. At small wave numbers, where buoyancy feeds energy to the velocity field, kinetic energy exhibits inverse cascade. Consequently, the kinetic energy spectrum scales as $k^{-11/5}$ and the kinetic energy flux shows $k^{-4/5}$ scaling at small wave numbers. Buoyancy is weakened at large wave numbers, and this leads to a constant enstrophy cascade and k^{-3} kinetic energy spectrum, similar to 2D hydrodynamic turbulence. However, the entropy spectrum exhibits a bispectrum with the upper branch varying as k^{-2}. We also observe constant entropy flux in the inertial range. Finally, we also draw a connection between the entropy flux in the dissipation range and the entropy dissipation rate in the bulk.

DOI: 10.1103/PhysRevFluids.9.023502

I. INTRODUCTION

Thermal convection is a widely encountered phenomenon in nature. The physics of convective flows is studied using the Rayleigh-Bénard setup, where a fluid is confined between a pair of parallel horizontal plates. The bottom plate is heated and the top plate is cooled. So the lighter hot fluid rises due to buoyancy while the heavier cold fluid falls [1–3]. Our understanding of the physics of thermal convection has grown steadily over the years [4–7]. However, the behavior of convective flows at very high Rayleigh numbers remains a subject of active research.

The strength of the convective flow is proportional to buoyancy forcing and inversely proportional to the dissipation in the fluid. The nondimensional parameter Rayleigh number (Ra) is used to denote the ratio between these counteracting forces. Consequently, high Ra convection is more turbulent and complex. The Prandtl number (Pr) is another parameter which represents the ratio of kinematic and thermal diffusivities. In the present study, we focus mainly on the effects of buoyancy at large Ra ranging from 10^{11} to 10^{14}, and we keep the value of Pr fixed at 1.

Understanding the nature of turbulent thermal convection and its energy transfers has been a challenge. Some researchers claim that thermal convection exhibits Bolgiano-Obukhov [8,9] (BO) phenomenology. Procaccia and Zeitak [10], L'vov [11] made early theoretical arguments for BO scaling in thermal convection. Subsequently, Yakhot [12] employed third-order velocity structure functions to predict BO scaling in Rayleigh-Bénard convection (RBC). Many

*roshanj@iitk.ac.in
†mkv@iitk.ac.in

 ©2024 American Physical Society

numerical and experimental works also reported the presence of BO scaling in thermal convection [13–18]. However, more recent works argue in favor of Kolmogorov-Obukhov [19] (KO) scaling in RBC [7,20–23]. Mishra and Verma [20] performed pseudospectral simulations of RBC and reported KO scaling for low and intermediate Prandtl numbers. Moreover, Bhattacharya *et al.* [22] demonstrated the similarities in structure functions of thermal convection and hydrodynamic turbulence to further bolster the arguments in support of KO scaling in RBC.

Numerous works have confirmed the predictions of BO phenomenology in stably stratified turbulence [21,24–26]. Kumar and Verma [25] and Alam *et al.* [26] used shell-model analysis to show that BO scaling holds for stable stratification. Moreover, Bhattacharjee [27] used a global energy balance analysis to further bolster the arguments of BO theory. Rosenberg *et al.* [28] performed high-resolution DNS of rotating turbulence with stratification and obtained spectra that agree with BO scaling. More recently, Basu and Bhattacharjee [29] showed that the BO regime is most prominent for moderate stratification as compared to weak or strong stratification. It was also shown by Bhattacharjee *et al.* [30] that the BO scaling observed in stably stratified fluids arises from the scale invariance of thermal flux.

Kumar *et al.* [21] and Verma *et al.* [7] showed that in 3D RBC, thermal plumes drive the velocity field, and as a result, the kinetic energy flux cannot decrease with increasing wave number. They also showed that for $\mathrm{Pr} \leqslant 1$, plumes primarily force the large-scale structures. Based on these arguments and detailed numerical simulations, they arrived at the conclusion that 3D RBC exhibits a $k^{-5/3}$ kinetic energy spectrum and constant kinetic energy flux.

Note, however, that in two dimensions, hydrodynamic turbulence displays an altogether different behavior. At small wave numbers, 2D hydrodynamics exhibit inverse cascade of kinetic energy. Two-dimensional hydrodynamic turbulence forced at intermediate scale exhibits constant energy flux and a $k^{-5/3}$ energy spectrum. However, 2D turbulent convection is forced at all scales by buoyancy. This forcing creates variations in the energy flux with wave number and deviation of the energy spectrum from $k^{-5/3}$ to $k^{-11/5}$. This is the basic theme of our paper. Building upon the presence of inverse energy cascade, Verma [3] argued that the magnitude of kinetic energy flux will increase as we move towards smaller wave numbers. Hence we may expect $|\Pi_u(k)| \sim k^{-4/5}$, as was predicted by Bolgiano [8] and Obukhov [9]. Consequently, one may expect Bolgiano-Obukhov scaling in 2D RBC, so that the kinetic energy spectrum scales as $E_u(k) \sim k^{-11/5}$. Note that Brandenburg [31] made a similar argument using shell models in the case of magnetoconvection. Mazzino [32] showed that the velocity and temperature structure functions of 2D convection follow Bolgiano-Obukhov (BO) scaling. More recently, Xie and Huang [33] derived structure function relations from the Kármán-Howarth-Monin equations for 2D isotropic convection. Their findings, backed by direct numerical simulations in a doubly periodic domain, also justified the existence of BO scaling in 2D convection. Stepanov *et al.* [34] also used shell models to demonstrate the feasibility of observing BO-scaling. The authors argue that a precise combination of factors is necessary to observe BO-scaling.

We expect turbulent convection to be inhomogeneous and anisotropic. However, Nath *et al.* [35] studied anisotropy in RBC using numerical simulations, and they showed that turbulent convection for a Prandtl number near unity is approximately isotropic. They computed the scale-by-scale anisotropy parameter, $A(k) = |\mathbf{u}_\perp(k)|^2/[2|u_\parallel(k)|^2]$, where $\mathbf{u}_\perp(k)$ and $u_\parallel(k)$ are velocity components perpendicular and parallel to the buoyancy direction. They showed that $A \approx 0.72$, and also that the ring spectrum for $\mathrm{Pr} \approx 1$ is nearly isotropic. Xie and Huang [33] also arrived at similar conclusions based on their structure function calculations. These observations justify the usage of shell spectra for turbulent convection.

Additionally, we also note that although the bulk flow in turbulent convection is reasonably homogeneous, the boundary layers are thin and inhomogeneous. However, the boundary layers contribute to the large wave numbers in the energy spectrum (exponential range), whereas the bulk flow contributes to the energy spectrum in the inertial range. We focus only on the inertial range spectrum in our present work. This further reinforces the applicability of the homogeneity approximation for Fourier transform and energy spectrum calculations [7]. Finally, we note that recent works have applied this approximation successfully to derive useful insights into thermal convection at a wide range of Prandtl numbers [36].

Note also that BO phenomenology argues for a dual spectrum for kinetic energy. Accordingly, $E_u(k)$ scales as $k^{-11/5}$ at small wave numbers due to buoyancy effects, whereas at larger wave numbers, $E_u(k) \sim k^{-5/3}$ since buoyancy is weakened at small scales. However, observing a dual spectrum requires very high-resolution simulations [26], which has been a challenge. Rosenberg *et al.* [28], however, observed a dual spectrum in their simulations of rotating stratified flows. Note that Zhu *et al.* [37] performed high-resolution simulations of 2D RBC and analyzed the heat transfer and boundary layers in detail, however a spectral analysis of energy and flux transfers remains to be performed. The simulations we present are based on a subset of the parameters used by Zhu *et al.* [37].

The conjecture that 2D RBC may exhibit BO scaling provides us with a unique opportunity to observe a dual-spectrum because extreme resolution DNS is easier to perform for 2D flows as compared to 3D flows. In this paper, we simulate 2D RBC on high-resolution grids with up to $12\,288 \times 12\,288$ grid points, and we observe the dual spectrum of $k^{-11/5}$ and k^{-3}, in line with the predictions of BO phenomenology.

The outline of the paper is as follows. In Sec. II, we briefly outline the governing equations and review the Bolgiano-Obukhov phenomenology in the context of 2D RBC. We then describe our numerical method, computational setup, and flow profiles in Sec. III. Subsequently in Sec. IV, we present our results demonstrating the presence of BO scaling in 2D RBC. In Sec. V, we focus on the transfer and dissipation of entropy in 2D high Ra convection. Specifically, we study how the dissipation of entropy in the boundary layer is related to the global entropy flux. We summarize our findings and conclude the paper in Sec. VI.

II. SPECTRAL PHENOMENOLOGY OF 2D RBC

We solve the following nondimensionalized equations of Rayleigh-Bénard convection (RBC) [3]:

$$\frac{\partial \mathbf{u}}{\partial t} + \mathbf{u} \cdot \nabla \mathbf{u} = -\nabla p + T\hat{z} + \sqrt{\frac{\mathrm{Pr}}{\mathrm{Ra}}}\nabla^2 \mathbf{u}, \tag{1}$$

$$\frac{\partial T}{\partial t} + \mathbf{u} \cdot \nabla T = \sqrt{\frac{1}{\mathrm{RaPr}}}\nabla^2 T. \tag{2}$$

$$\nabla \cdot \mathbf{u} = \mathbf{0}. \tag{3}$$

Here $\mathbf{u}$, p, and T are the velocity, pressure, and temperature fields, respectively. The above equations have been nondimensionalized by the free-fall velocity $u_f = \sqrt{\alpha g \Delta H}$, the imposed temperature difference Δ, and the domain height H. The nondimensional parameters are Rayleigh number $\mathrm{Ra} = \alpha g \Delta H^3/(\nu\kappa)$ and Prandtl number $\mathrm{Pr} = \nu/\kappa$. Additionally, α is the bulk thermal expansion coefficient, g is the acceleration due to gravity, and ν and κ are the kinematic viscosity and thermal diffusivity, respectively.

We use periodic boundary conditions in the horizontal direction, and no-slip, conducting plates at the top and bottom in the present study. Furthermore, we apply the Boussinesq approximation to neglect density variations everywhere except for the buoyancy forcing term on the right side of the momentum equation. The validity of the Boussinesq approximation at the high Rayleigh numbers considered in this study is contingent on the properties of the working fluid used in the Rayleigh-Bénard cell. By choosing the physical dimensions of the domain and material properties of the fluid appropriately, it is possible to attain high Rayleigh numbers without having compressibility effects interfere with the physics of the flow.

We now briefly review the turbulence phenomenology by Bolgiano [8] and Obukhov [9], which was originally applied to stably stratified flows. We start with the kinetic energy equation in one-dimensional wave-number space [3,38],

$$\frac{\partial}{\partial t}E_u(k,t) = T_u(k,t) + F_B(k,t) - D_u(k,t) = -\frac{\partial}{\partial k}\Pi_u(k,t) + F_B(k,t) - D_u(k,t). \tag{4}$$

Here, $E_u(k,t)$ is the total kinetic energy of the Fourier modes lying within the wave-number shell of radius k, defined as

$$E_u(k) = \frac{1}{2}\sum_{k\leqslant|\mathbf{k}'|<k+1} |\mathbf{u}(\mathbf{k}')|^2. \tag{5}$$

$\Pi_u(k,t)$ is the kinetic energy flux, which is the energy leaving via nonlinear triad interactions from a sphere of radius k, the energy injection rate by buoyancy is represented by $F_B(k,t)$ (defined below), and $D_u(k,t) = 2\nu k^2 E_u(k,t)$ is the energy dissipation rate. The nonlinear energy transfer $T_u(\mathbf{k}) = \widehat{\mathbf{u}\cdot\nabla\mathbf{u}}(\mathbf{k})$, where $\widehat{f}$ represents Fourier transform of f.

Following similar lines, we define the entropy spectrum $E_\theta(k)$ for the temperature fluctuations from the mean, $\theta(\mathbf{r}) = T(\mathbf{r}) - T_m(z)$, where $T_m(z)$ is the linear temperature drop. Similar to Eq. (4), the evolution equation for the entropy spectrum is [3]

$$\frac{\partial}{\partial t}E_\theta(k,t) = -\frac{\partial}{\partial k}\Pi_\theta(k,t) + F_\theta(k,t) - D_\theta(k,t). \tag{6}$$

The entropy spectrum and flux terms in the above equation are written as

$$E_\theta(k) = \frac{1}{2}\sum_{k\leqslant|\mathbf{k}'|<k+1} |\theta(\mathbf{k}')|^2, \quad \Pi_\theta(k) = -\int_0^k T_\theta(k')dk', \tag{7}$$

where $T_\theta(\mathbf{k}) = \widehat{\mathbf{u}\cdot\nabla\theta}(\mathbf{k})$ is the nonlinear transfer term for θ. Finally, $F_\theta(k,t)$ represents the entropy injection rate, and $D_\theta(k,t)$ is the entropy dissipation spectrum, defined as

$$D_\theta(k) = -2\kappa k^2 E_\theta(k). \tag{8}$$

We do not focus on entropy injection and dissipation spectra in this paper. Returning to Eq. (4), the kinetic energy input by buoyancy is denoted by $F_B(k,t)$,

$$F_B(k) = \sum_{k\leqslant|\mathbf{k}'|<k+1} \mathcal{R}[\mathbf{u}(\mathbf{k},t)\cdot\mathbf{f}_B^*(\mathbf{k},t)] = \sum_{k\leqslant|\mathbf{k}'|<k+1} \mathcal{R}[u_z(\mathbf{k},t)\theta^*(\mathbf{k},t)]. \tag{9}$$

Here $\mathcal{R}$ represents the real part of the complex term, and $\mathbf{f}_B^*(\mathbf{k},t)$ is the complex conjugate of $\mathbf{f}_B(\mathbf{k},t)$, which denotes the buoyancy force.

In the inertial range, dissipation is negligible, hence $D_u(k,t) = 0$. Therefore, under steady state, over the inertial range, we have

$$\frac{d}{dk}\Pi_u(k) = F_B(k). \tag{10}$$

For stably stratified turbulence, Bolgiano [8] and Obukhov [9] argued that $F_B(k) < 0$ since kinetic energy gets converted to potential energy. Hence,

$$\frac{d}{dk}\Pi_u(k) < 0. \tag{11}$$

Using dimensional analysis, Bolgiano [8] and Obukhov [9] showed that at small wave numbers (inertial range), the kinetic energy spectrum varies as $k^{-11/5}$, while the kinetic energy flux varies as $k^{-4/5}$. This can be obtained from a force balance between the nonlinear and buoyancy terms of Eq. (1) in Fourier space,

$$ku_k^2 = \rho_k g, \tag{12}$$

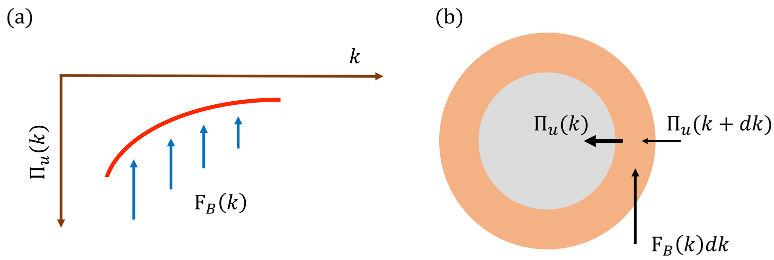

FIG. 1. For 2D RBC, (a) a schematic diagram of energy injection rate by buoyancy [$F_B(k)$]. (b) Because of inverse cascade of kinetic energy, $|\Pi_u(k)|$ is larger than $|\Pi_u(k+dk)|$. That is, $|\Pi_u(k)|$ decreases with k (adapted from Verma [3]).

where u_k and ρ_k are the Fourier transforms of the velocity field and density fluctuation field, respectively. Note that the buoyancy force denoted by $T\hat{z}$ in Eq. (1) can also be written as $-\rho g\hat{z}$, which is the form used to write Eq. (12). It is also assumed that the potential energy flux Π_ρ is constant in the inertial range, so that

$$\Pi_\rho(k) = k\rho_k^2 u_k = \epsilon_\rho. \tag{13}$$

From Eqs. (12) and (13), with a bit of algebra, it can be shown that

$$E_u(k) = \frac{u_k^2}{k} = c_1\epsilon_\rho^{2/5} g^{4/5} k^{-11/5}, \tag{14}$$

$$\Pi_u(k) = ku_k^3 = c_2\epsilon_\rho^{3/5} g^{6/5} k^{-4/5}. \tag{15}$$

This phenomenology is referred to as *Bolgiano-Obukhov scaling*. Note that the above phenomenology is for three-dimensional flow. In the case of thermal convection, however, the temperature field feeds the kinetic energy. Hence, $F_B(k) > 0$, and [3,7,21]

$$\frac{d}{dk}\Pi_u(k) > 0. \tag{16}$$

But numerical simulations of Kumar *et al.* [21] and Verma *et al.* [7] have shown that $\Pi_u(k)$ is still nearly constant across the inertial range, due to two major factors—the kinetic energy input by buoyancy is restricted to low wave numbers, and the remaining effect of buoyancy gets canceled out by viscous drag [3,7]. However, in the case of 2D RBC, we have an inverse cascade of kinetic energy [39], so that $\Pi_u(k) < 0$ at low wave numbers [see Fig. 1(a)]. Based on this observation, Verma [3] conjectured that 2D RBC may obey BO scaling. The argument is as follows. In RBC, buoyancy feeds the kinetic energy, hence $F_B(k) > 0$. Therefore, inverse cascade of kinetic energy leads to

$$|\Pi_u(k)| > |\Pi_u(k+dk)|. \tag{17}$$

That is, $|\Pi_u(k)|$ decreases with wave number, as shown in Fig. 1(a). Now, following similar arguments as in Bolgiano [8] and Obukhov [9], we can argue that

$$E_u(k) = \epsilon_\theta^{3/5} k^{-11/5}, \tag{18}$$

$$\Pi_u(k) = \epsilon_\theta^{3/5} k^{-4/5}, \tag{19}$$

$$\Pi_\theta(k) = \epsilon_\theta, \tag{20}$$

where ϵ_θ is the entropy dissipation rate, which is defined as

$$\epsilon_\theta = \int \kappa|\nabla\theta|^2 dV. \tag{21}$$

We remark that the entropy spectrum for RBC exhibits a bispectrum, wherein we observe two branches—with the upper branch scaling as k^{-2} and the lower branch following neither $k^{-5/3}$ nor $k^{-7/5}$ [7]. Thus, it does not follow the original BO scaling (see Sec. V).

For stably stratified turbulence, Bolgiano [8] and Obukhov [9] argued that buoyancy effects become negligible at large wave numbers, and $E_u(k) \sim k^{-5/3}$ (Kolmogorov's spectrum). Note, however, that at large wave numbers, 2D hydrodynamic turbulence exhibits

$$E_u(k) = K'_{2D}\epsilon_\omega^{2/3}k^{-3}, \tag{22}$$

$$\Pi_\omega(k) = \epsilon_\omega, \tag{23}$$

where $\Pi_\omega(k)$ and ϵ_ω are enstrophy flux and dissipation rates, respectively. Here, $K'_{\rm 2D}$ is a constant whose value is approximately 1.1–1.7 [40]. Note that enstrophy, which is defined as

$$E_\omega = \int (\nabla \times \mathbf{u})^2 d\mathbf{r}, \tag{24}$$

is conserved in 2D inviscid hydrodynamic flows. Motivated by the above observation, we expect that 2D RBC should exhibit $E_u(k) \sim k^{-3}$ and constant enstrophy flux at large wave numbers, as in Eqs. (22) and (23). Combining the above, we argue that 2D RBC should exhibit BO scaling, and its energy and entropy should follow Eqs. (18)–(20) for small wave numbers, and Eqs. (22) and (23) for large wave numbers.

Bolgiano [8] and Obukhov [9] showed that the transition between $k^{-11/5}$ and $k^{-5/3}$ occurs at Bolgiano wave number k_B. The corresponding lengthscale, $l_B = 1/k_B$, is given by [2]

$$l_B = \epsilon_u^{5/4}\epsilon_\theta^{-3/4}. \tag{25}$$

The above formula assumes a transition of kinetic energy flux from $k^{-4/5}$ to constant. Note, however, that in 2D RBC, enstrophy flux is expected to be constant at large wave numbers. Therefore, we employ an alternative formula for k_B based on the energy injection rate, which is

$$k_B = \frac{\int kF_B(k)dk}{\int F_B(k)dk}. \tag{26}$$

With this formula, k_B represents a wave number beyond which buoyancy is weak. We find that the above formula provides a reasonable fit to our numerical data (see Sec. IV A).

Structure functions too play an important role in quantifying turbulence phenomenologies [19,41]. The nth-order velocity structure function is evaluated using the longitudinal velocity difference

$$\delta\mathbf{u}(\mathbf{r}) = [\mathbf{u}(\mathbf{x} + \mathbf{r}) - \mathbf{u}(\mathbf{r})] \cdot \mathbf{r}/r, \tag{27}$$

where $r = |\mathbf{r}|$. Ching [42] and others have derived structure functions for the velocity field in BO turbulence phenomenology. Based on dimensional analysis, it can be derived that for large lengthscales (or small wave numbers) where $k^{-11/5}$ scaling holds,

$$S_3^u(r) = \langle(\delta\mathbf{u})^3\rangle \sim \epsilon_\theta^{3/5}r^{9/5}, \tag{28}$$

$$S_2^u(r) = \langle(\delta\mathbf{u})^2\rangle \sim \epsilon_\theta^{2/5}r^{6/5}. \tag{29}$$

The positive sign of $S_3^u(r)$ indicates inverse cascade of kinetic energy for the inertial range where $k^{-11/5}$ scaling is applicable. We will verify the above scaling numerically.

In Sec. IV, we verify BO scaling for 2D RBC. We remark that observing the BO dual spectra requires simulations at extreme resolutions, and such studies have been rare so far [26]. Earlier, Rosenberg *et al.* [28] had reported dual scaling for rotating stratified turbulence, but their range of the power law was rather limited. In this paper, we report dual spectra of BO phenomenology using two-dimensional simulations on very fine grids (up to 150 million grid-points).

TABLE I. Details of Rayleigh number Ra, aspect ratio Γ, grid sizes, total simulation times in free-fall units, $t_{\max}$, and Reynolds number, Re.

Ra	Γ	Grid	$t_{\max}$	Re
10^{11}	2	4096×2048	500	188440 ± 3140
10^{12}	2	8192×4096	120	446770 ± 3100
10^{13}	2	16384×8192	90	1164400 ± 24300
10^{14}	1	12288×12288	25	3440900 ± 6500

III. COMPUTATIONAL DETAILS AND FLOW STRUCTURES

We use a finite-difference solver derived from SARAS [43,44] for our simulations. The MPI-parallel solver uses a collocated configuration wherein the velocity, temperature, and pressure fields are all positioned at the cell-centers. All spatial derivatives are computed with fourth-order accuracy, except in the pressure correction step, which uses second-order accurate operators. To resolve the very thin boundary layers near the top and bottom plates, we use a nonuniform grid generated by a tangent-hyperbolic function along the z-direction. This ensures that we retain at least 10 points in the boundary layer even at the highest Rayleigh numbers (see Table III). The grid is uniform in the horizontal periodic direction.

Structure of convective flow

We performed four simulations of RBC at Ra ranging from 10^{11} to 10^{14}, and a fixed $\mathrm{Pr} = 1$. The computational domain is a 2D box of height H and length L, and the aspect ratio of the box is defined as $\Gamma = L/H$. The first three cases have $\Gamma = 2$, whereas the last case has $\Gamma = 1$ in order to reduce the computational cost. At the bottom and top plates, we impose no-slip boundary condition on velocity, and fixed-temperature (conducting) boundary condition on temperature. The domain is periodic in the horizontal direction. The parameters we use are similar to those studied by Zhu *et al.* [37]. The details of the cases are listed in Table I.

In Fig. 2, we show the structure of flow fields at times selected from statistical steady-state regime of the convective flow. Figures 2(a)–2(d) correspond to Rayleigh numbers 10^{11}, 10^{12}, 10^{13}, and 10^{14}, respectively. The instantaneous temperature fields are shown with red (blue) regions corresponding to hot (cold) fluid packets. We have limited the range of nondimensionalized temperature to a narrow band of $(0.45, 0.55)$ to show the bulk flow structure clearly. In each plot, we observe that there is one distinct upwelling of hot fluid and a corresponding downflow of cold fluid from the bottom and top plates, respectively.

The presence of large-scale circulation (LSC) in the form of coherent convecting roll(s) is noticeable in all four cases. Moreover, the thickness of the plumes decreases as the Ra increases, resulting in an increasingly fine-grained structure, characteristic of highly turbulent flows. Also, the thermal boundary layers become vanishingly thin at very high Ra, and it is barely visible in frames (c) and (d). This aspect is important for the spectral analysis, which will be discussed in Sec. IV A.

We will now investigate the spectra, fluxes, and structure functions of 2D RBC in the forthcoming sections. In all the plots that we show and discuss henceforth, we use a common color scheme for consistency. All lines and markers corresponding to the Rayleigh numbers 10^{11}, 10^{12}, 10^{13}, and 10^{14} use the colors blue, green, red, and cyan, respectively.

IV. BOLGIANO-OBUKHOV SCALING IN 2D RBC

We now verify BO scaling in 2D RBC using numerical simulations. We compute the kinetic energy spectrum and flux, the second- and third-order velocity structure functions, as well as the Bolgiano wave number.

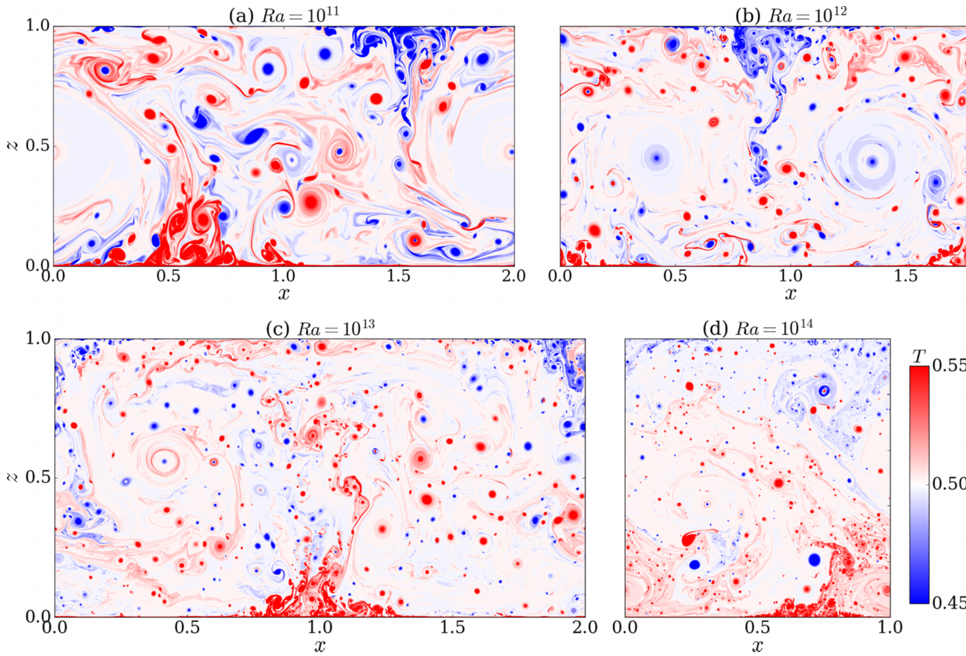

FIG. 2. Contour plots of the temperature field for the four cases from Table I. In the top row, we show the filled contours for Ra $= 10^{11}$ (a) and 10^{12} (b). In the bottom row, we show the fields at Ra $= 10^{13}$ (c) and 10^{14} (d). In each case, we observe one distinct upwelling of hot fluid from the bottom plate and a corresponding downflow of cold fluid from the top plate.

A. Kinetic energy spectrum and flux

We compute the kinetic energy spectra $E_u(k)$ for the four cases listed in Table I using the formula of Eq. (5). Note that we use the free-slip basis functions for computing the spectra and fluxes. A possible concern regarding Fourier analysis of RBC is the inhomogeneity of the system in the vertical direction. As noted in Sec. III A where the flow structures were presented, the boundary layers near the top and bottom walls tend to be quite thin at high Rayleigh numbers like the ones considered here. Hence, the structures within the boundary layers are very small compared to the box height, and they would contribute only to the large wave-number regime of the spectra. So, it is safe to conclude that the boundary layer will not affect the inertial range properties significantly. Therefore, the inertial-range energy and entropy spectra computed using free-slip basis functions are quite close to those of realistic flows [3]. Finally, we also perform time-averaging of the computed spectra over the period of time in statistical steady-state. We plot $E_u(k)$ in Fig. 3 and show that it clearly exhibits dual spectra, $k^{-11/5}$ and k^{-3}, which is consistent with the model described in Sec. II. The spectra in Fig. 3 exhibit approximately a decade each of $k^{-11/5}$ and k^{-3} regimes. Such a clear separation of the dual scaling regimes is, to the best of our knowledge, a novel result in numerical simulations of RBC. We attribute this to the very high resolution grids used in the present study.

We also evaluate the scale-by-scale anisotropy parameter, $A(k) = E_\perp(k)/E_\parallel(k)$, for 2D turbulent convection at high Ra, and we plot them in Fig. 4. Here, $E_\perp(k)$ and $E_\parallel(k)$ are the contributions to the total kinetic energy from the velocity components perpendicular and parallel to the buoyancy direction, respectively. We adopt the same procedure as the one outlined in Nath *et al.* [35] for computing $A(k)$. Within the inertial range, $A(k) \approx 1$, indicating that the flow is fairly isotropic at large scales. The increasing anisotropy at small scales ($k \gg 1$) can be attributed to the dissipation occurring close to the walls. However, the uniformity of the large-scale flow structures justifies the

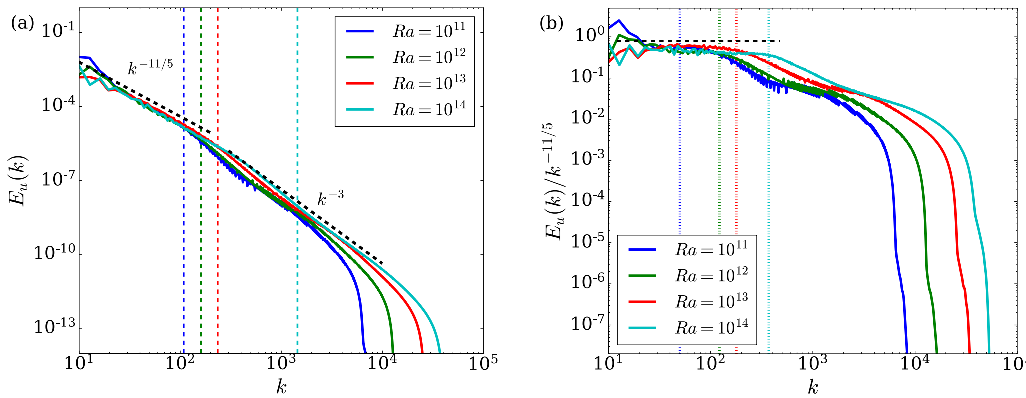

FIG. 3. Time-averaged spectra of kinetic energy for $10^{11} \leqslant \mathrm{Ra} \leqslant 10^{14}$. The spectra scale as $k^{-11/5}$ at low wave numbers and as k^{-3} at higher wave numbers. We plot $E_u(k)$ in (a), and the compensated spectrum $E_u(k)/k^{-11/5}$ in (b). The vertical dashed (a) and dotted (b) lines represent k_B computed from Eqs. (26) and (25), respectively. The k_B computed for each Ra are matched by their respective colors.

applicability of shell-spectra for analyzing energy transfers in 2D thermal convection at large Ra and Pr $= 1$.

Next, we compute the Bolgiano wave number k_B using the kinetic energy injection rate F_B as described in Eq. (26). To understand the dynamics in detail, we plot $F_B(k)$ versus k in Fig. 5(a). The range over which $F_B(k)$ shows a constant slope matches approximately with that of $E_u(k) \sim k^{-11/5}$ in Fig. 3. In Table II, we tabulate the values of k_B computed using the formulas given by Eqs. (25) and (26). To compare the two approaches for computing k_B, we turn to the plots shown in Figs. 3(a) and 3(b). The vertical dashed lines plotted in Fig. 3(a) correspond to the values of k_B obtained from Eq. (26), whereas the dotted lines in Fig. 3(b) are computed from Eq. (25). We observe that for Ra $= 10^{12}$ and 10^{13}, the two approaches agree rather satisfactorily. However, Eq. (25) underpredicts k_B for Ra $= 10^9$, and Eq. (26) overpredicts k_B for Ra $= 10^{14}$. We believe that the difference in the

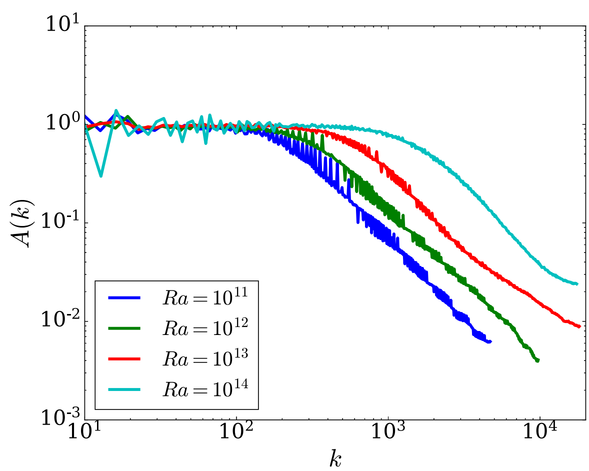

FIG. 4. Scale-by-scale anisotropy parameter $A(k) = E_\perp(k)/E_\parallel(k)$ for $10^{11} \leqslant \mathrm{Ra} \leqslant 10^{14}$ as computed by Nath *et al.* [35]. We note that $A(k) \approx 1$ within the inertial range, indicating that the flow is isotropic. This further justifies the applicability of shell spectra for analyzing 2D turbulent thermal convection for the range of parameters considered here.

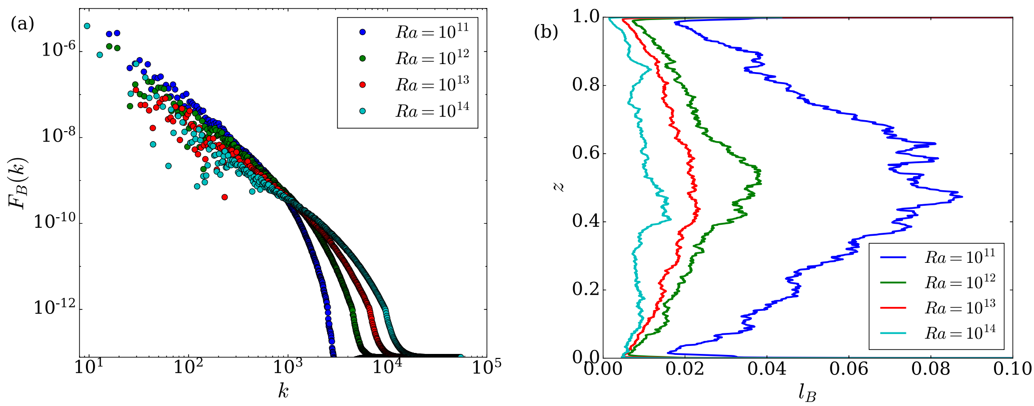

FIG. 5. Energy injection spectrum (a), $F_b(k)$, for Ra = 10^{11}, 10^{12}, 10^{13}, and 10^{14}. The spectra display a nearly constant slope approximately until the Bolgiano wave number. Moreover, the slopes decrease with increasing Ra, indicating a wider range of scales affected by buoyancy. This also points to a corresponding increase in k_B. The variation of local Bolgiano lengthscale (b) indicates that l_B is maximum towards the center of the convection cell.

two l_B is due to the assumption of constant Π_u made in the formula given by Eq. (25). Additionally, the computation of ϵ_u is susceptible to numerical errors as noted by Pandey *et al.* [45]. Specifically, it was noted that the calculation of the strain-rate tensor S_{ij} on finite-difference grids magnifies the effect of grid discretization errors [46].

Another relevant observation is that the value of l_B is not constant throughout the domain. Benzi *et al.* [47], for instance, introduced a local Bolgiano lengthscale by taking the planar average of Eq. (25). They noted that l_B grows within the bulk of the convection cell, attaining a maximum close to the center of the cell. Here we compute the local l_B using the same procedure, and we plot its profile along the z-axis in Fig. 5(b). Note that for the moderate Ra $= 10^7$ considered in [47], the maximum l_B at the cell center was nearly the size of the cell. For the very high Ra we take in the present work, however, the maximum l_B is significantly smaller than the cell-size. Moreover, this maximum value decreases with increasing Ra, which is consistent with the increasing value of k_B seen in Fig. 3. The minimum value of l_B is encountered at the outer edge of the boundary layer, consistent with the observation by Benzi *et al.* [47].

We now compute the kinetic energy flux by first computing the nonlinear energy transfer function $T_u(k)$ as described in Sec. II. For the computation of $T_u(k)$ from numerical data, we employ second-order finite-difference schemes to compute the nonlinear term. The numerical errors incurred in this operation somewhat contaminate the computed $T_u(k)$. Moreover, the solution data sets are stored over a nonuniform grid, which is finer near the walls and coarser in the bulk. When computing the Fourier transform, the data are first interpolated onto a uniform grid, because the FFT

TABLE II. Estimations of the Bolgiano lengthscale and wave number for Ra = 10^{11}, 10^{12}, 10^{13}, and 10^{14}. We compare the two methods of calculating l_B described in Sec. IV here.

Ra	k_B [$F_B(k)$]	l_B [$F_B(k)$]	l_B (ϵ)
10^{11}	108.1	9.2×10^{-3}	2.0×10^{-2}
10^{12}	160.9	6.2×10^{-3}	8.2×10^{-3}
10^{13}	234.7	4.2×10^{-3}	5.6×10^{-3}
10^{14}	1446.2	6.9×10^{-4}	2.7×10^{-3}

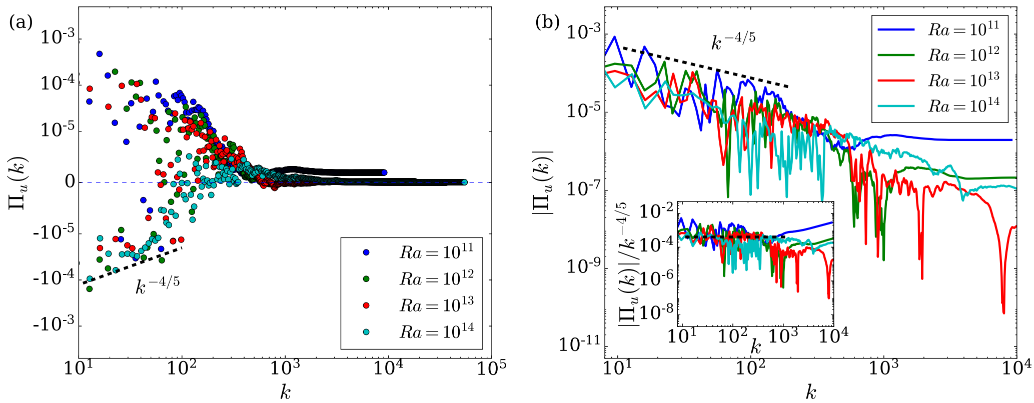

FIG. 6. (a) Time-averaged fluxes of kinetic energy for $\mathrm{Ra} = 10^{11}$, 10^{12}, 10^{13}, and 10^{14}. Although the spectrum varies smoothly with k, the flux shows a wide scatter due to the numerical errors in computing $T_u(k)$. In the range where $E_u \sim k^{-11/5}$, we note that $\Pi_u \sim k^{-4/5}$. This is visible more clearly in (b), which shows the absolute value of the kinetic energy flux, $|\Pi_u(k)|$. In the inset, we also plot the compensated $|\Pi_u(k)|/k^{-4/5}$ flux to show the constant slope of the flux barring the fluctuations from numerical errors in computing the transfer function and flux.

algorithm requires its input to be uniformly spaced. This interpolation step also contributes to the errors in $T_u(k)$. In spite of these errors, the computed values of $T_u(k)$ are reasonable.

We plot the $\Pi_u(k)$ computed thus in Fig. 6. As shown in the figure, $\Pi_u(k)$ fluctuates significantly taking positive and negative values, similar to those observed for 2D hydrodynamic turbulence [48]. Note, however, that $|\Pi_u(k)|$ appears to follow the $k^{-4/5}$ curve. Also, the negative values $\Pi_u(k)$ dominate the positive counterparts, thus yielding net negative kinetic energy flux. Also, note that $\Pi_u(k) \to 0$ for $k > 10^3$, similar to 2D hydrodynamic turbulence [40,48]. We also remark that structure functions provide much smoother plots to highlight the negative kinetic energy flux (see Sec. III A).

In this subsection, we have demonstrated the existence of dual kinetic energy spectra ($k^{-5/3}$ and k^{-3}) and $\Pi_u(k)\, k^{-4/5}$ at small wave numbers in 2D RBC. We will now analyze the enstrophy spectrum and flux in Sec. IV B.

B. Enstrophy spectrum and flux

In Sec. II, we argued that in 2D RBC, at large wave numbers, $E_u(k) \sim k^{-3}$ and enstrophy flux is constant. To verify the above argument, we compute the time-averaged enstrophy spectra and fluxes for the four runs, and we plot them in Figs. 7(a) and 7(b), respectively.

We show the normalized enstrophy spectrum $kE_\omega(k)$ in Fig. 7(a). We observe a flat regime over a range around $k \approx 10^3$, which is consistent with the range over which $E_u(k) \sim k^{-3}$ in Fig. 3. This indicates that $E_\omega \sim k^{-1}$. This is consistent with the k^{-3} scaling observed for $E_u(k)$, since $E_u(k) \sim E_\omega/k^2$.

The corresponding enstrophy flux plots are exhibited in Fig. 7(b). These plots show an approximately constant $\Pi_\omega(k)$ for $k > 10^3$. Interestingly, $\Pi_\omega(k) \sim k^{6/5}$ for $10^2 < k < 10^3$, which corresponds to

$$\Pi_u(k) \sim \Pi_\omega/k^2 \sim k^{-4/5}. \tag{30}$$

This scaling governs the kinetic energy flux at smaller wave numbers. These two observations are consistent with the BO scaling for 2D RBC discussed in Sec. II.

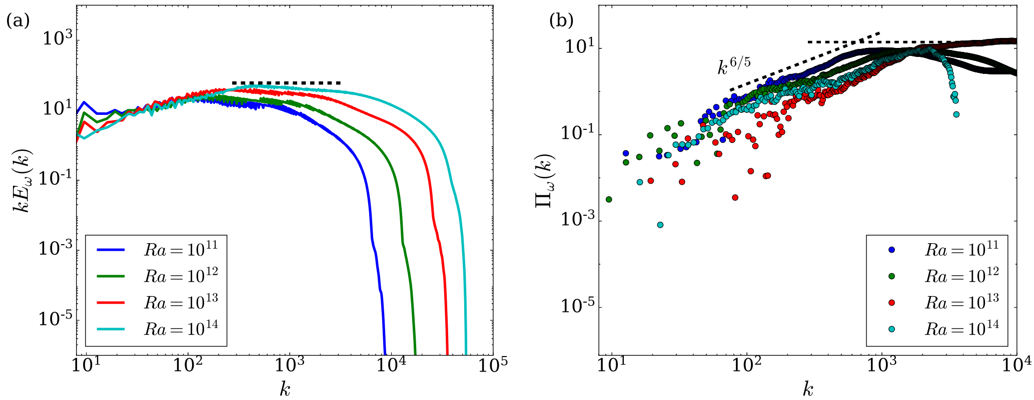

FIG. 7. For 2D RBC with $\mathrm{Ra} = 10^{11}$, 10^{12}, 10^{13}, and 10^{14}, (a) time-averaged normalized enstrophy spectrum, $kE_\omega(k)$, and (b) enstrophy flux, $\Pi_\omega(k)$. In (b), the regions with constant Π_ω are marked with dashed horizontal lines. The $k^{6/5}$ line represents the region where $E_u(k) \sim k^{-11/5}$.

C. Structure functions

Continuing our justification for BO scaling in 2D thermal convection, we now analyze the structure functions computed using our simulation data sets. Computing structure functions is a computationally expensive task, and we use a GPU accelerated Python code for the calculations presented in this subsection. This code is derived from the fastSF C++ script developed at our laboratory [49].

We compute S_2^u and S_3^u [see Eqs. (27)–(29)] using the data sets and perform time-averaging. Even with an optimized GPU-parallelized code, we found that computing the two-point statistical quantities over grids with as many as 150 million points takes an exorbitant amount of time. As a result, we interpolate our solutions to coarser grids to compute the structure functions. A similar strategy to improve computation times of the structure function was also used by Verdini *et al.* [50]. The data sets from $\mathrm{Ra} = 10^{11}$, 10^{12}, and 10^{13} simulations were interpolated to a 1024×512 grid, and the $\mathrm{Ra} = 10^{14}$ data set was similarly reduced to a 768×768 grid. Thus, we focus on the behavior of structure functions only at moderate and large r values that correspond to $E_u(k) \sim k^{-11/5}$ scaling.

In Fig. 8(a), we plot the third-order velocity structure function $S_3(r)$ normalized by $-\epsilon_\theta^{3/5} r^{9/5}$. We compute ϵ_θ using Eq. (21). As shown in the figure, we observe that $S_3(r) \propto r^{9/5}$ for $r > 0.1$. In addition, $S_3(r) > 0$ indicating inverse cascade of kinetic energy at large r or small k. Moreover, the normalized $S_3(r)$ is of the order 1, as clarified by the dashed horizontal lines at $y = \pm 1$ in the figure. Furthermore, in Fig. 8(b), we plot $S_2(r)$ normalized by $-\epsilon_\theta^{2/5} r^{6/5}$ against r to show the lengthscales with $r^{6/5}$ scaling. Thus, the scaling of $S_2(r)$ and $S_3(r)$ is consistent with the predictions of BO scaling for the kinetic energy.

In the next section, we compute the entropy spectrum and flux using the temperature data. We will show that entropy flux is constant for 2D RBC, consistent with the predictions of BO phenomenology.

V. ENTROPY SPECTRUM AND FLUX

We compute the entropy spectrum $E_\theta(k)$ and the entropy flux $\Pi_\theta(k)$ using Eq. (7) introduced earlier in Sec. II. The entropy spectra are plotted in Fig. 9. The spectrum $E_\theta(k)$ exhibits a bispectrum, as observed previously for thermal convection in 3D domains [3,7,20]. Here, the upper branch varies as k^{-2}, whereas the lower branch does not follow a fixed scaling law. It has been shown analytically that the k^{-2} scaling of the upper branch arises from the mean temperature profile, which

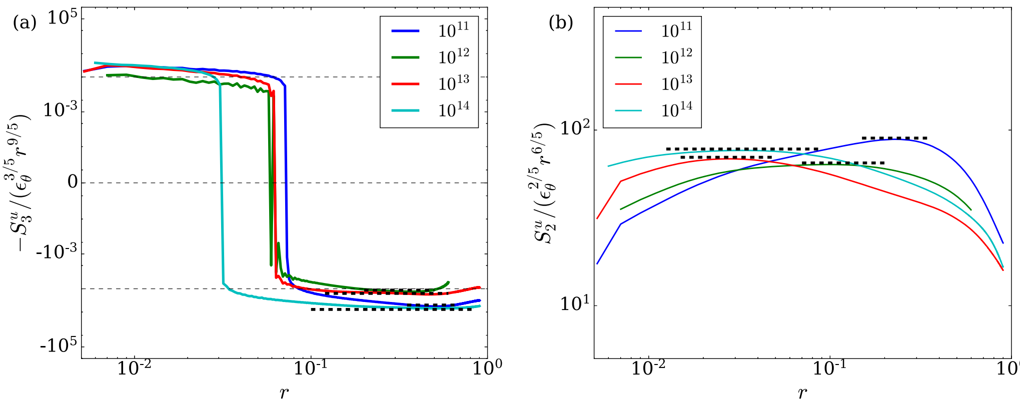

FIG. 8. (a) Third-order structure functions of velocity for Ra $= 10^{11}$, 10^{12}, 10^{13}, and 10^{14}. The plots are compensated by $\epsilon_\theta^{3/5} r^{9/5}$ to highlight the region where the BO scaling of $S_3^u \sim r^{9/5}$ is obeyed. For each case, there is a distinct inversion of energy cascade as expected from the dual scaling seen earlier in the kinetic energy spectra of Fig. 3. The dashed horizontal lines at $y = \pm 1$ indicate that the normalized $S_3(r)$ is of order 1. (b) The corresponding second-order structure functions for the four cases. Again we have marked with dashed black lines the approximate regions with BO scaling of $S_2^u \sim r^{6/5}$.

is represented by the $\theta(0, k)$ modes that vary as k^{-1} [3,51]. We also draw attention to the fact that the lower branch tends to become steeper with increasing Rayleigh number. At the lowest Ra of 10^{11}, the lower branch approximately scales as $k^{-0.32}$, whereas at the highest Ra of 10^{14}, the lower branch is steeper and scales as $k^{-0.67}$. This could be a consequence of the increased thermal fluctuations dominating the bulk flow at higher Rayleigh numbers.

The entropy flux, $\Pi_\theta(k)$, is plotted in Fig. 10. We note that for all Rayleigh numbers, there is a range of wave numbers over which the flux is constant. This is in agreement with the predictions of BO theory. Moreover, the length of this inertial range increases with Ra due to the increasing intensity of turbulence and corresponding Reynolds number. Interestingly, we note that at the point where the inertial range ends and the flux begins to drop, all the curves have a common tangent.

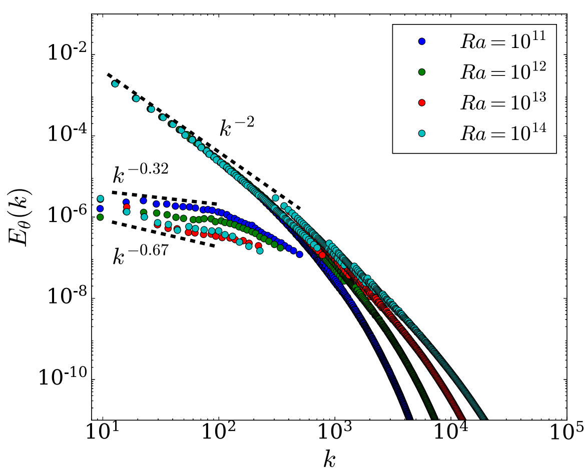

FIG. 9. Time-averaged entropy spectrum, $E_\theta(k)$, for Ra $= 10^{11}$, 10^{12}, 10^{13}, and 10^{14}. The spectra show dual scaling as due to the differing effects of the mean temperature profile and temperature fluctuations [3].

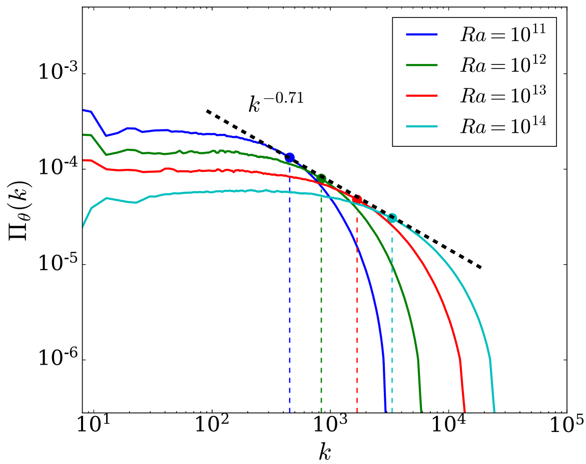

FIG. 10. Time-averaged entropy flux for $10^{11} \leqslant \mathrm{Ra} \leqslant 10^{14}$. The entropy flux shows a universal slope of $k^{-0.71}$ close to the dissipation range that spans the three decades of Ra considered here.

We have plotted this tangent with a dashed black line in the figure. Moreover, this tangent scales as $k^{-0.71}$ approximately.

Note that we have marked filled circles at the approximate points where the tangent line touches the curves. Each filled circle is colored to correspond with the curve on which it lies. We have also marked the points on the k-axis corresponding to each tangent point. The significance of these points will be explained next.

Interestingly, the tangent of the entropy flux plots in Fig. 10 is linked to the entropy dissipation rate in the boundary layer. To justify this argument, we analyze the thermal boundary layer profiles

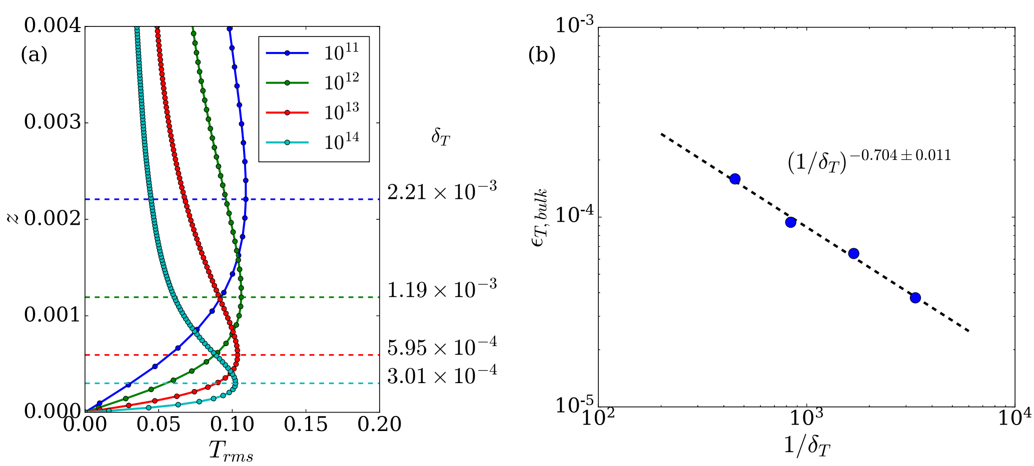

FIG. 11. (a) Thermal boundary layer profiles in terms of T_{rms} plotted near the bottom walls for the six cases listed in Table I. Each profile is obtained by taking the time-average of the individual T_{rms} computed for each solution data set after attaining steady-state. The exact values of the thermal boundary layer heights (taken as maxima of the T_{rms} profiles) are written on the right side of the plot. (b) Scaling of entropy dissipation in the bulk $\epsilon_{\theta,\mathrm{bulk}}$ against the inverse of thermal boundary layer thickness, $1/\delta_T$. The slope of the fit-line is such that it scales as 0.704 ± 0.011, which is very close to the slope of the tangent obtained earlier in Fig. 10.

TABLE III. Details of Rayleigh number Ra, thermal boundary layer resolution in terms of number of points N_{δ_T}, height of the thermal boundary layer δ_T, wave number corresponding to thermal boundary layer thickness k_{δ_T}, entropy dissipation in the bulk $\epsilon_{\theta,\text{bulk}}$, and in the boundary layer $\epsilon_{\theta,\text{BL}}$. Selected quantities from this table are plotted in Fig. 11.

Ra	N_{δ_T}	δ_T	k_{δ_T}	$\epsilon_{\theta,\text{bulk}}$	$\epsilon_{\theta,\text{BL}}$
10^{11}	13	2.21×10^{-3}	452.8	1.59×10^{-4}	4.58×10^{-4}
10^{12}	14	1.19×10^{-3}	838.0	9.39×10^{-5}	2.67×10^{-4}
10^{13}	14	5.95×10^{-4}	1681.7	6.43×10^{-5}	1.57×10^{-4}
10^{14}	11	3.01×10^{-4}	3324.8	3.76×10^{-5}	9.86×10^{-5}

plotted in Fig. 11(a). We compute the time-averaged T_{rms}, defined as

$$T_{\text{rms}}(z) = \langle \sqrt{\langle [T(x,z,t) - \langle T(x,z,t)\rangle_x]^2 \rangle_x} \rangle_t. \tag{31}$$

In the figure, the above function has been plotted close to the bottom wall for different Rayleigh numbers.

The markers on each of the lines indicate the grid points, and they provide an estimate of the number of points at different distances from the bottom plate. We relate the maxima of these curves to the upper limit of the thermal boundary layers. As expected, the thickness of the thermal boundary layer, δ_T, decreases with increasing Ra. We have listed the values of δ_T both in Fig. 11(a) as well as in Table III.

We observe that δ_T is linked to the scaling of the tangent line observed in the entropy flux plots of Fig. 10. The points on the k-axis corresponding to the tangent points (marked with dashed vertical lines) are in fact $k_{\delta_T} = 1/\delta_T$. We have also listed the numerical values of k_{δ_T} in Table III for reference. This indicates that the tangent points represent the thermal boundary layer cutoff in the entropy flux. Consequently, the value of Π_θ which corresponds to each tangent point should indicate the entropy dissipation rate in the bulk, $\epsilon_{\theta,\text{bulk}}$. Note that the entropy dissipation rates in the bulk and boundary layer are

$$\epsilon_{\theta,\text{bulk}} = \frac{\kappa}{V}\int_{V_{\text{bulk}}} |\nabla\theta|^2 dV, \quad \epsilon_{\theta,\text{BL}} = \frac{\kappa}{V}\int_{V_{\text{BL}}} |\nabla\theta|^2 dV. \tag{32}$$

Here κ is the thermal diffusivity, and V_{bulk}, V_{BL}, and V are the volumes (areas in the case of our 2D simulations) of the bulk, boundary layer, and entire domain, respectively. Consequently, $\epsilon_{\theta,\text{bulk}} + \epsilon_{\theta,\text{BL}} = \epsilon_\theta$. This division of dissipation rates into bulk and boundary layer regions is consistent with earlier theoretical analyses performed by Grossmann and Lohse [52] and Bhattacharya *et al.* [53]. Note also that all the quantities are time-averaged as well. Indeed, we find that when we plot $\epsilon_{\theta,\text{bulk}}$ against $1/\delta_T$, as shown in Fig. 11(b), we observe a scaling of $k^{-0.704\pm0.011}$, which is satisfactorily close to the $k^{-0.71}$ scaling seen in Fig. 10.

In Table III, we have listed the entropy dissipation rates in the boundary layer, $\epsilon_{\theta,\text{BL}}$, as well. We also note that in the range of Ra considered in this study, $\epsilon_{\theta,\text{BL}}$ is 2.3–2.9 times greater than $\epsilon_{\theta,\text{bulk}}$. A similar ratio was also observed by Bhattacharya *et al.* [53] for $10^5 \leqslant \text{Ra} \leqslant 10^9$ and $0.02 \leqslant \text{Pr} \leqslant 100$. However, theoretical studies on the scaling of global quantities in RBC [52] have predicted that at very high Rayleigh numbers, the dissipation rate in the bulk will be greater than that in the boundary layer. This prediction is based on the fact that as Ra increases, the thermal boundary layer becomes thinner, resulting in a diminished contribution to the overall thermal dissipation. However, we observe that although the boundary layer does indeed get significantly thinner at high Ra (Fig. 11), the temperature gradient also increases concomitantly, such that $\epsilon_{\theta,\text{BL}}$ remains higher than $\epsilon_{\theta,\text{bulk}}$ throughout the range of Ra considered in the present work. Whether this trend reverses at a still higher Ra remains to be investigated, at least in the case of $\text{Pr} = 1$ flows.

VI. DISCUSSION AND CONCLUSIONS

It has been shown previously that 3D turbulent convection exhibits Kolmogorov-like scaling. However, turbulence phenomenology of 2D thermal convection remains speculative. We perform DNS of 2D RBC at very high grid resolutions of up to $12\,288 \times 12\,288$, with unit Prandtl number and Ra ranging from 10^{11} to 10^{14}. The numerically computed kinetic energy exhibits a $k^{-11/5}$ spectrum at small wave numbers and a k^{-3} spectrum at large wave numbers. The absolute kinetic energy flux scales as $|\Pi_u(k)| \sim k^{-4/5}$ at small wave numbers, while enstrophy flux is constant at large wave numbers. Note that buoyancy is active at small wave numbers, but is negligible at large wave numbers. These observations indicate Bolgiano-Obukhov scaling for 2D RBC.

Consistent with the Bolgiano-Obukhov scaling, the entropy flux is constant in the inertial range. However, the entropy spectrum exhibits a bispectrum. The upper branch scales as k^{-2} due to the linear temperature profile along the vertical [3]. The entropy spectrum in lower branch varies from $k^{-0.32}$ to $k^{-0.67}$ with the increase of Ra.

Interestingly, in the entropy flux, the transition wave number from the inertial range to the dissipation range follows a curve that scales as $\approx k^{-0.71}$. We show that this scaling law arises due to the division of entropy dissipation between the bulk and boundary layer. We also observe that the thermal dissipation is consistently high in the boundary layer as compared to the bulk. More importantly, this characteristic persists even with increasing Ra.

ACKNOWLEDGMENTS

We thank the late Professor Ravi Samtaney for his valuable guidance in developing the SARAS solver and for securing compute time on the Shaheen supercomputer. We thank Harshit Negi and Avinash Jha for their help in spectrum and flux calculations at the incipient stages of our work. We also thank Soumyadeep Chatterjee for his useful inputs on flux and structure function calculations. We thank Mohammed Anas for his insightful comments on thermal convection. Our numerical simulations were performed on Cray XC40 (Shaheen II) of KAUST supercomputing laboratory, Saudi Arabia, through Project No. k1416. The support and the resources provided by PARAM Sanganak under the National Supercomputing Mission, Government of India at the Indian Institute of Technology, Kanpur are also gratefully acknowledged.

APPENDIX: NUMERICAL METHOD

We solve the governing equations [Eqs. (1)–(3)] using a third-order semi-implicit Runge-Kutta method [54]. In this method, the equations are split into their linear and nonlinear components, $\mathcal{L}$ and $\mathcal{N}$, respectively. The nonlinear, pressure, and forcing terms are time-advanced explicitly, while the diffusion terms are treated semi-implicitly [54]. In this framework, we perform three substeps to compute $\mathbf{u}_{n+1}$ from $\mathbf{u}_n$:

$$\mathbf{u}' = \mathbf{u}_n + \Delta t[\mathcal{L}(\alpha_1 \mathbf{u}_n + \beta_1 \mathbf{u}') + \gamma_1 \mathcal{N}(\mathbf{u}_n)], \tag{A1}$$

$$\mathbf{u}'' = \mathbf{u}' + \Delta t[\mathcal{L}(\alpha_2 \mathbf{u}' + \beta_2 \mathbf{u}'') + \gamma_2 \mathcal{N}(\mathbf{u}') + \zeta_1 \mathcal{N}(\mathbf{u}_n)], \tag{A2}$$

$$\mathbf{u}_{n+1} = \mathbf{u}'' + \Delta t[\mathcal{L}(\alpha_3 \mathbf{u}'' + \beta_3 \mathbf{u}_{n+1}) + \gamma_3 \mathcal{N}(\mathbf{u}'') + \zeta_2 \mathcal{N}(\mathbf{u}')]. \tag{A3}$$

Here, α_i, β_i, γ_i, and ζ_j for $i = 1, 2, 3$ and $j = 1, 2$ are parameters obtained from Spalart *et al.* [55] and Orlandi [56]. The nonlinear term is written in a semiconservative form by taking a weighted sum of its divergence and advective forms,

$$\mathbf{u} \cdot \nabla \mathbf{u} = \frac{1}{2}\left(u_j \frac{\partial u_i}{\partial x_j}\right) + \frac{1}{2}\frac{\partial}{\partial x_j}(u_i u_j). \tag{A4}$$

This form is called the skew symmetric form [57] and it stabilizes the solver greatly. We use a predictor-corrector method at each substep of RK3. Each step is thus composed of two substeps, wherein we first calculate a predicted value of the velocity field, $\mathbf{u}^*$. We use a vectorized Jacobi iterative solver to calculate $\mathbf{u}^*$. Using the predicted velocity field, we solve the pressure Poisson equation to compute the pressure correction,

$$\nabla^2 p_c = \frac{\nabla \cdot \mathbf{u}^*}{(\alpha_1 + \beta_1)\Delta t}. \tag{A5}$$

The above elliptic equation is solved iteratively, and this step takes a major fraction of our computing time. There are a variety of iterative solvers available for this task, and we find that the multigrid method yields fast convergence and accurate results [58,59]. We use a V-cycle based geometric multigrid solver [59]. This solver was developed in-house for tight integration with the SARAS solver. The solver relies on Red-Black Gauss-Seidel (RBGS) iterator for both the smoothing steps at individual V-cycle subgrids as well as for solving the equation at the coarsest level. The RBGS method adds to the fast convergence with multithreaded vectorized calculations. We then update pressure with the correction term, and correct the predicted velocity field to satisfy divergence:

$$p' = p_n + p_c, \quad \mathbf{u}' = \mathbf{u}^* - \Delta t(\alpha_1 + \beta_1)\nabla p_c. \tag{A6}$$

Note here that only the velocity and pressure fields are changed in the corrector step. The temperature field at the next substep, T', is obtained directly from the predictor step without any need for correction. Finally, we impose boundary conditions on $\mathbf{u}'$, p', and T'. The above steps are repeated for each substep of RK3, Eqs. (A2) and (A3), to finally obtain $\mathbf{u}_{n+1}$, p_{n+1}, and T_{n+1}.

[1] A. V. Getling, *Rayleigh-Bénard Convection: Structures and Dynamics* (World Scientific, Singapore, 1998).

[2] D. Lohse and K.-Q. Xia, Small-scale properties of turbulent Rayleigh–Bénard convection, Annu. Rev. Fluid Mech. **42**, 335 (2010).

[3] M. K. Verma, *Physics of Buoyant Flows: From Instabilities to Turbulence* (World Scientific, Singapore, 2018).

[4] E. D. Siggia, High Rayleigh number convection, Annu. Rev. Fluid Mech. **26**, 137 (1994).

[5] G. Ahlers, S. Grossmann, and D. Lohse, Heat transfer and large scale dynamics in turbulent Rayleigh-Bénard convection, Rev. Mod. Phys. **81**, 503 (2009).

[6] F. Chillà and J. Schumacher, New perspectives in turbulent Rayleigh-Bénard convection, Eur. Phys. J. E **35**, 58 (2012).

[7] M. K. Verma, A. Kumar, and A. Pandey, Phenomenology of buoyancy-driven turbulence: recent results, New J. Phys. **19**, 025012 (2017).

[8] R. Bolgiano Jr., Turbulent spectra in a stably stratified atmosphere, J. Geophys. Res. **64**, 2226 (1959).

[9] A. M. Obukhov, On influence of buoyancy forces on the structure of temperature field in a turbulent flow, Dokl. Acad. Nauk SSSR **125**, 1246 (1959).

[10] I. Procaccia and R. Zeitak, Scaling exponents in nonisotropic convective turbulence, Phys. Rev. Lett. **62**, 2128 (1989).

[11] V. S. L'vov, Spectra of velocity and temperature-fluctuations with constant entropy flux of fully-developed free-convective turbulence, Phys. Rev. Lett. **67**, 687 (1991).

[12] V. Yakhot, 4/5 Kolmogorov law for statistically stationary turbulence: Application to high-Rayleigh-number Bénard convection, Phys. Rev. Lett. **69**, 769 (1992).

[13] X.-Z. Wu, L. Kadanoff, A. Libchaber, and M. Sano, Frequency power spectrum of temperature fluctuations in free convection, Phys. Rev. Lett. **64**, 2140 (1990).

[14] R. Benzi, F. Massaioli, S. Succi, and R. Tripiccione, Scaling behaviour of the velocity and temperature correlation functions in 3D convective turbulence, Europhys. Lett. **28**, 231 (1994).

[15] R. Benzi, R. Tripiccione, F. Massaioli, S. Succi, and S. Ciliberto, On the scaling of the velocity and temperature structure functions in Rayleigh-Bénard convection, Europhys. Lett. **25**, 341 (1994).

[16] L. Skrbek, J. J. Niemela, K. R. Sreenivasan, and R. J. Donnelly, Temperature structure functions in the Bolgiano regime of thermal convection, Phys. Rev. E **66**, 036303 (2002).
[17] E. Calzavarini, F. Toschi, and R. Tripiccione, Evidences of Bolgiano-Obhukhov scaling in three-dimensional Rayleigh-Bénard convection, Phys. Rev. E **66**, 016304 (2002).
[18] R. P. J. Kunnen, H. J. H. Clercx, B. J. Geurts, L. J. A. van Bokhoven, R. A. D. Akkermans, and R. Verzicco, Numerical and experimental investigation of structure-function scaling in turbulent Rayleigh-Bénard convection, Phys. Rev. E **77**, 016302 (2008).
[19] A. N. Kolmogorov, Dissipation of Energy in Locally Isotropic Turbulence, Dokl. Acad. Nauk SSSR **32**, 16 (1941).
[20] P. K. Mishra and M. K. Verma, Energy spectra and fluxes for Rayleigh-Bénard convection, Phys. Rev. E **81**, 056316 (2010).
[21] A. Kumar, A. G. Chatterjee, and M. K. Verma, Energy spectrum of buoyancy-driven turbulence, Phys. Rev. E **90**, 023016 (2014).
[22] S. Bhattacharya, S. Sadhukhan, A. Guha, and M. K. Verma, Similarities between the structure functions of thermal convection and hydrodynamic turbulence, Phys. Fluids **31**, 115107 (2019).
[23] M. K. Verma, Variable energy flux in turbulence, J. Phys. A **55**, 013002 (2022).
[24] Y. Kimura and J. R. Herring, Diffusion in stably stratified turbulence, J. Fluid Mech. **328**, 253 (1996).
[25] A. Kumar and M. K. Verma, Shell model for buoyancy-driven turbulence, Phys. Rev. E **91**, 043014 (2015).
[26] S. Alam, A. Guha, and M. K. Verma, Revisiting bolgiano–obukhov scaling for moderately stably stratified turbulence, J. Fluid Mech. **875**, 961 (2019).
[27] J. K. Bhattacharjee, Kolmogorov argument for the scaling of the energy spectrum in a stratified fluid, Phys. Lett. A **379**, 696 (2015).
[28] D. L. Rosenberg, A. G. Pouquet, R. Marino, and P. D. Mininni, Evidence for Bolgiano-Obukhov scaling in rotating stratified turbulence using high-resolution direct numerical simulations, Phys. Fluids **27**, 055105 (2015).
[29] A. Basu and J. K. Bhattacharjee, Kolmogorov or bolgiano-obukhov scaling: Universal energy spectra in stably stratified turbulent fluids, Phys. Rev. E **100**, 033117 (2019).
[30] J. K. Bhattacharjee, A. Kumar, and M. K. Verma, Turbulence in a stably stratified fluid: onset of global anisotropy as a function of the richardson number, Phys. Scr. **94**, 125008 (2019).
[31] A. Brandenburg, Energy-spectra in a model for convective turbulence, Phys. Rev. Lett. **69**, 605 (1992).
[32] A. Mazzino, Two-dimensional turbulent convection, Phys. Fluids **29**, 111102 (2017).
[33] J.-H. Xie and S.-D. Huang, Bolgiano–obukhov scaling in two-dimensional isotropic convection, J. Fluid Mech. **942**, A19 (2022).
[34] R. Stepanov, A. Shestakov, and P. Frick, Feasibility of the Obukhov-Bolgiano scaling in buoyancy affected turbulence, Phys. Rev. Fluids **8**, L052601 (2023).
[35] D. Nath, A. Pandey, A. Kumar, and M. K. Verma, Near isotropic behavior of turbulent thermal convection, Phys. Rev. Fluids **1**, 064302 (2016).
[36] S. Bhattacharya, M. K. Verma, and R. Samtaney, Prandtl number dependence of the small-scale properties in turbulent rayleigh-bénard convection, Phys. Rev. Fluids **6**, 063501 (2021).
[37] X. Zhu, V. Mathai, R. J. A. M. Stevens, R. Verzicco, and D. Lohse, Transition to the Ultimate Regime in Two-Dimensional Rayleigh-Bénard Convection, Phys. Rev. Lett. **120**, 144502 (2018).
[38] P. A. Davidson, *Turbulence: An Introduction for Scientists and Engineers* (Oxford University Press, Oxford, 2004).
[39] R. H. Kraichnan, Inertial ranges in two-dimensional turbulence, Phys. Fluids **10**, 1417 (1967).
[40] G. Boffetta and R. E. Ecke, Two-Dimensional Turbulence, Annu. Rev. Fluid Mech. **44**, 427 (2012).
[41] A. N. Kolmogorov, The local structure of turbulence in incompressible viscous fluid for very large Reynolds numbers, Dokl. Acad. Nauk SSSR **30**, 301 (1941).
[42] E. S. C. Ching, *Statistics and Scaling in Turbulent Rayleigh-Bénard Convection* (Springer, Berlin, 2013).
[43] R. Samuel, S. Bhattacharya, A. Asad, S. Chatterjee, M. K. Verma, R. Samtaney, and S. F. Anwer, SARAS: A general-purpose PDE solver for fluid dynamics, J. Open Source Software **6**, 2095 (2021).
[44] M. K. Verma, R. Samuel, S. Chatterjee, S. Bhattacharya, and A. Asad, Challenges in fluid flow simulations using exascale computing, SN Comput. Sci. **1**, 178 (2020).

[45] A. Pandey, D. Krasnov, K. R. Sreenivasan, and J. Schumacher, Convective mesoscale turbulence at very low prandtl numbers, J. Fluid Mech. **948**, A23 (2022).
[46] A. Viré and B. Knaepen, On discretization errors and subgrid scale model implementations in large eddy simulations, J. Comput. Phys. **228**, 8203 (2009).
[47] R. Benzi, F. Toschi, and R. Tripiccione, On the heat transfer in rayleigh–bénard systems, J. Stat. Phys. **93**, 901 (1998).
[48] A. Gupta, R. Jayaram, A. G. Chaterjee, S. Sadhukhan, R. Samtaney, and M. K. Verma, Energy and enstrophy spectra and fluxes for the inertial-dissipation range of two-dimensional turbulence, Phys. Rev. E **100**, 053101 (2019).
[49] S. Sadhukhan, S. Bhattacharya, and M. K. Verma, fastSF: A parallel code for computing the structure functions of turbulence, J. Open Source Software **6**, 2185 (2021).
[50] A. Verdini, R. Grappin, P. Hellinger, S. Landi, and W. C. Müller, Anisotropy of third-order structure functions in mhd turbulence, Astrophys. J. **804**, 119 (2015).
[51] A. Pandey and M. K. Verma, Scaling of large-scale quantities in Rayleigh-Bénard convection, Phys. Fluids **28**, 095105 (2016).
[52] S. Grossmann and D. Lohse, Scaling in thermal convection: a unifying theory, J. Fluid Mech. **407**, 27 (2000).
[53] S. Bhattacharya, M. K. Verma, and R. Samtaney, Revisiting Reynolds and Nusselt numbers in turbulent thermal convection, Phys. Fluids **33**, 015113 (2021).
[54] W. Cheng and R. Samtaney, A high-resolution code for large eddy simulation of incompressible turbulent boundary layer flows, Comput. Fluids **92**, 82 (2014).
[55] P. R. Spalart, R. D. Moser, and M. M. Rogers, Spectral methods for the Navier-Stokes equations with one infinite and two periodic directions, J. Comput. Phys. **96**, 297 (1991).
[56] P. Orlandi, *Fluid Flow Phenomena: A Numerical Toolkit* (Springer Science & Business Media, Dordrecht, Netherlands, 2000), Vol. 55.
[57] Y. Morinishi, T. Lund, O. Vasilyev, and P. Moin, Fully conservative higher order finite difference schemes for incompressible flow, J. Comput. Phys. **143**, 90 (1998).
[58] P. Wesseling, *An Introduction to Multigrid Methods* (Wiley, West Sussex, UK, 1995).
[59] W. L. Briggs, V. E. Henson, and S. F. McCormick, *A Multigrid Tutorial* (SIAM, Philadelphia, USA, 2000).